J. Fluid Mech. (1974), *vol.* 66, *part* 2, *pp.* 353–376
Printed in Great Britain

Steady simple shear flow past a circular cylinder at moderate Reynolds numbers: a numerical solution

By CHARLES A. KOSSACK† AND ANDREAS ACRIVOS

Department of Chemical Engineering, Stanford University, Stanford, California 94305

(Received 29 October 1973)

The two-dimensional steady flow of an incompressible viscous fluid past a circular cylinder, placed symmetrically in a simple shear field, has been studied for both the stationary and the freely rotating case by solving numerically the Navier–Stokes equations for values of the Reynolds number R in the range

$$0{\cdot}047 \leqslant R \leqslant 70.$$

At $R = 0{\cdot}047$, the present results are in substantial agreement with the analytic small-R perturbation solution given by Robertson & Acrivos (1970). Inertia effects were found, however, to play a significant role even at $R = 1$, and hence the calculated flow pattern for $R \geqslant 1$ differs significantly from that of the creeping-flow solution. Specifically, for the freely rotating case, the region of closed streamlines decreases rapidly in extent with increasing R, two symmetrically placed wakes are formed on either side of the cylinder and the dimensionless rotational speed of the freely suspended cylinder decreases as $R^{-\frac{1}{2}}$. In fact, for a value of R as low as 70, many of the gross features of the flow are surprisingly similar to those described by an inviscid solution except for the difference in the two sets of pressure profiles and the fact that the numerical results do not as yet exhibit the expected flow separation on the surface of the cylinder.

1. Introduction

Problems involving the motion of small spheres and cylinders freely suspended in a non-uniform flow field have received considerable attention in the last few years, not only because of their importance from a fundamental point of view, but also because their solution constitutes the first step in understanding many complex phenomena such as the flow of red cells in the blood and of fibre suspensions in paper making, the lateral migration of solid as well as deformable particles suspended in Poiseuille flow, the rheology of emulsions and the associated problem of mass transfer between the continuous and discrete phases, plus many more. Up to now, however, most of the studies on the subject, experimental as well as theoretical, appear to have been limited to small values of the Reynolds number,

† Present address, Atlantic Richfield Company, Dallas, Texas.

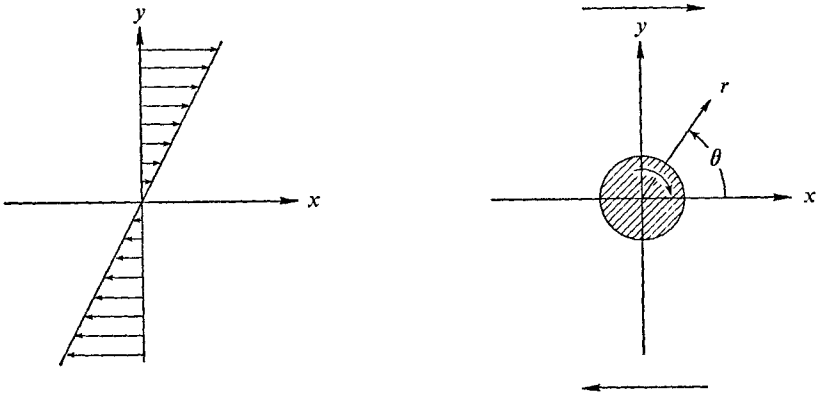

FIGURE 1. The undisturbed simple shear flow and the location of the cylinder in the flow field.

the result being that many of the effects arising from the presence of large inertia forces have remained unexplored. Here we attempt to fill this void for the case of a circular cylinder freely suspended in a simple shear flow, by presenting numerical solutions to the Navier–Stokes equations for values of the shear Reynolds number up to 70.

The system to be considered, shown schematically in figure 1, consists of a circular cylinder of radius a placed symmetrically in a simple shear flow whose rate of strain is denoted by S. The Reynolds number R is defined as $R \equiv Sa^2/\nu$, with ν the kinematic viscosity of the fluid, and all velocities and lengths are rendered dimensionless using, respectively, Sa as the characteristic velocity and a as the characteristic length. Thus, the steady flow obeys the familiar dimensionless Navier–Stokes equations in terms of the stream function ψ and the vorticity ω

$$\nabla^2\psi = -\omega, \quad D\omega/Dt = R^{-1}\nabla^2\omega, \tag{1.1}$$

plus the boundary conditions

$$\psi = 0 \quad \text{at} \quad r = 1; \quad \hat{\omega} \equiv \omega + 1 \to 0, \quad \frac{1}{r}\hat{\psi} \equiv \frac{1}{r}\left(\psi - \frac{r^2}{2}\sin^2\theta\right) \to 0 \quad \text{as} \quad r \to \infty, \tag{1.2}$$

as well as the periodicity condition

$$\{\psi(r,\theta), \omega(r,\theta)\} = \{\psi(r,\theta+\pi), \omega(r,\theta+\pi)\}, \tag{1.3}$$

which arises from the symmetry of the flow. In the above, r and θ are the conventional cylindrical polar co-ordinates, with θ increasing counter-clockwise as shown in figure 1. Finally, the requirement of zero torque can be shown to reduce to

$$\Omega = \tfrac{1}{2} - \frac{1}{2\pi}\int_{-\frac{1}{2}\pi}^{\frac{1}{2}\pi} \hat{\omega}(r,\theta)\,d\theta, \tag{1.4}$$

$\Omega \equiv -u_\theta = \partial\psi/\partial r$ at $r = 1$ being the dimensionless speed with which the cylinder rotates.

The creeping-flow solution to the above, given by

$$\psi_0 = \tfrac{1}{2}r^2\sin^2\theta - \tfrac{1}{4}\{1 + (r^{-2} - 2)\cos 2\theta\}, \quad \Omega = \tfrac{1}{2}, \tag{1.5}$$

is well known, and the predicted flow pattern has been verified experimentally, for small values of R, by Cox, Zia & Mason (1968) and by Robertson & Acrivos (1970). For larger R, however, essentially nothing has been reported to date regarding the structure of the flow, except for the analysis by Robertson & Acrivos (1970), where a solution to (1.1)–(1.3) was developed for small but finite R. This was accomplished using the technique of matched asymptotic expansions, which led to the following two expressions for the stream function ψ satisfying the appropriate matching requirement in the overlap region.

(*a*) An 'inner' solution for $1 \leqslant r \leqslant O(R^{-\frac{1}{2}})$:

$$\psi = \psi_0(r,\theta) + R\ln R\psi_1(r,\theta) + R\psi_2(r,\theta) + o(R), \tag{1.6}$$

where analytic formulae were given by Robertson & Acrivos for the functions ψ_1 and ψ_2.

(*b*) An 'outer' solution for $O(R^{-\frac{1}{2}}) \leqslant r \leqslant \infty$ of the form

$$R\psi = \tfrac{1}{2}\rho^2\sin^2\theta + R\Psi(\rho,\theta) + O(R^2\ln R), \quad \rho \equiv R^{\frac{1}{2}}r,$$

when $\Psi(\rho,\theta)$ is the solution to

$$Y\frac{\partial\hat{\omega}}{\partial X} = \hat{\nabla}^2\hat{\omega}, \quad \hat{\nabla}^2\Psi = -\hat{\omega}, \quad (X,Y) \equiv (R^{\frac{1}{2}}x, R^{\frac{1}{2}}y), \quad \hat{\nabla} \equiv \frac{\partial^2}{\partial X^2} + \frac{\partial^2}{\partial Y^2}, \tag{1.7}$$

which matches with (1.6) and satisfies the last two conditions in (1.2) as $\rho \to \infty$.

Moreover, it was shown by Robertson & Acrivos that, for a freely rotating cylinder,

$$\Omega = \tfrac{1}{2}\{1 - 0{\cdot}2886R + O(R^2\ln R)\}. \tag{1.8}$$

It is recognized, of course, that the above expressions, being expansions of the appropriate exact solution about $R = 0$, may not provide a reliable description of the flow beyond a certain small value of R. Nevertheless, they do suggest certain trends in the evolution of the flow pattern with increasing R which, as will be seen later, are borne out to a surprising extent by the numerical solution even for R as large as 70.

Specifically, if (1.6), the stream function for the 'inner' solution, is evaluated for $R = 0{\cdot}047$, the resulting streamline pattern, depicted in figure 2, is seen to differ significantly from that arising from the creeping-flow solution (1.5) (cf. figures 8 and 9 of Robertson & Acrivos). For example, the region of closed streamlines, which is known to dominate the rate of heat or mass transfer from the cylinder at large values of the Péclet number (Frankel & Acrivos 1968), is now finite rather than infinite in extent and is followed, on either side, by a wake, i.e. a region of negative ψ, whose width is monotonically increasing with r; in fact, the pattern is qualitatively similar to that arising under creeping-flow conditions when the cylinder is in a state of hindered rotation, i.e. when $\Omega < \frac{1}{2}$ (cf. figure 7 of Robertson & Acrivos). It is moreover evident from (1.8) that, according to the perturbation solution, Ω should be expected to decrease monotonically with R and to become small in relation to the vorticity of the undisturbed shear flow when R is not much larger than $O(1)$. Thus, the analysis by Robertson & Acrivos would tend to indicate that, even for moderate values of R, the flow will be dominated by inertia effects and that its structure will bear little resemblance to that of the $R = 0$ solution as given by (1.5).

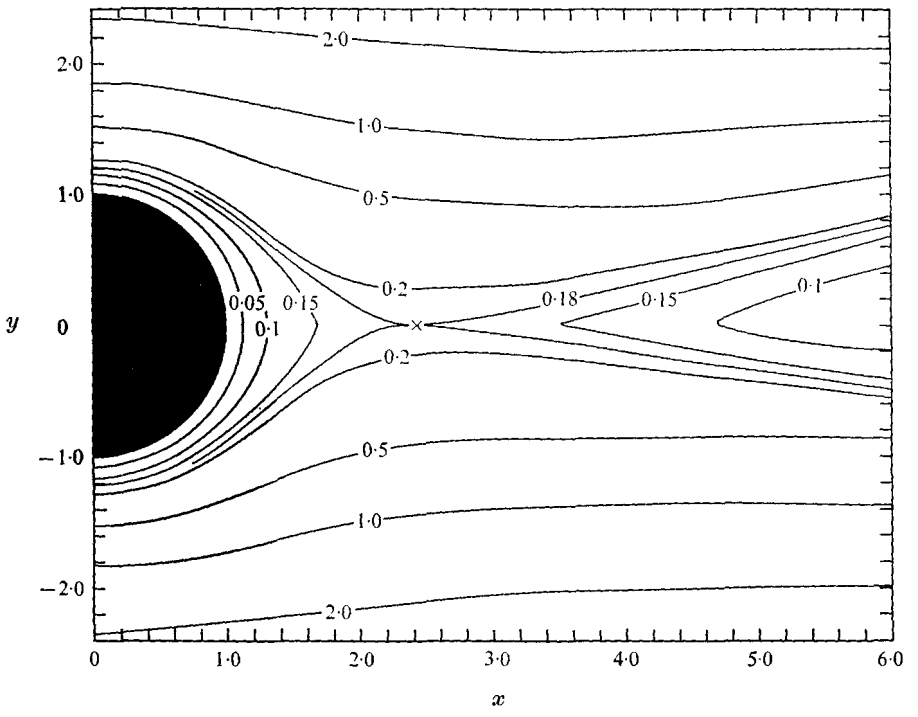

FIGURE 2. Stream-function field for zero torque, $R = 0{\cdot}047$ and $\Omega = 0{\cdot}49316$, obtained analytically from the inner solution.

It is also of some interest to solve the inviscid form of (1.1) in the hope that at least some of the features of this solution will be retained by the true streamline pattern when $R \gg 1$. With the viscous terms in (1.1) set, then, identically equal to zero, this pair of equations reduces to

$$\omega \equiv -1 = -\nabla^2\psi,$$

whose solution satisfying (1.2) is

$$\psi = \tfrac{1}{2}r^2\sin^2\theta - \tfrac{1}{4} - b\ln r + (4r^2)^{-1}\cos 2\theta, \tag{1.9}$$

b being a constant. To obtain its value, as well as that of Ω, it is necessary to examine the boundary-layer equations, which describe the flow in the immediate vicinity of the cylinder, subject to the conditions

$$u_\theta = -\Omega \quad \text{at} \quad r = 1, \quad u_\theta \to u_\infty(\theta) \quad \text{at the edge of the boundary layer,}$$

where, in view of (1.9),

$$u_\infty(\theta) = \cos 2\theta - (\tfrac{1}{2} - b).$$

Fortunately, a solution, which would be cumbersome to obtain, is not required in the present case, because the symmetric flow about $\theta = 0$, obtained by setting $b = \frac{1}{2}$, automatically satisfies the zero-torque condition (1.4) with $\Omega = 0$. To be sure, it is unlikely that this inviscid solution, which is sketched in figure 3, correctly represents the true flow pattern at high R, since a conventional

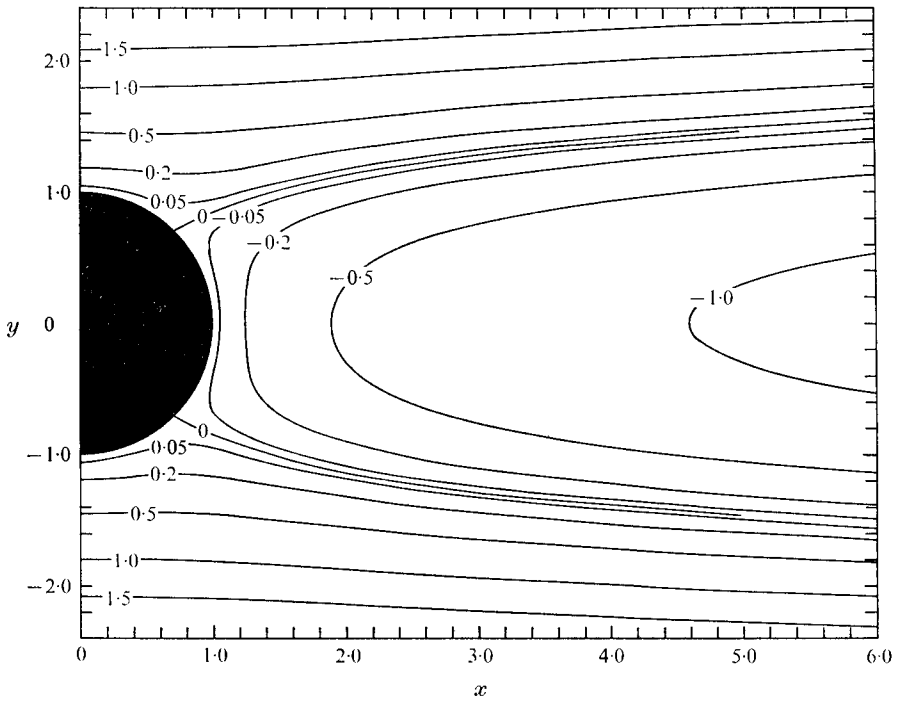

FIGURE 3. The inviscid solution (1.9) with $b = \frac{1}{2}$.

boundary-layer calculation with $\Omega = 0$ and $u_\infty(\theta) = \cos 2\theta = \sin(2\theta + \frac{1}{2}\pi)$ leads to the prediction (cf. Schlichting 1968, p. 161) that the boundary layer will separate at $\theta = 45° \pm 36°$. Nevertheless, it is of some interest that the gross features of this solution, for example a zero value for Ω, plus the presence of two wakes whose width increases logarithmically with r, are consistent with the trends predicted by the small-R analysis discussed above.

On the basis of both the small-R and the inviscid solutions, one would expect therefore that, with increasing R, Ω should decrease monotonically to zero and that a wake, qualitatively similar to that shown in figure 3, should form, extending from almost the surface of the cylinder to infinity. It will be seen that, indeed, the numerical calculations are in accord with these predictions.

2. The numerical technique

Before proceeding with the description of our numerical technique for solving (1.1) subject to (1.2)–(1.4), it is of some importance to examine in more detail the expected behaviour of the solution as $r \to \infty$. To this end we note that, far from the cylinder, the function $\hat{\omega} \equiv \omega + 1$ satisfies the first relation in (1.7), whose fundamental solution vanishing at infinity is (Bretherton 1962)

$$\zeta = \int_0^\infty \frac{dt}{2t(1+\frac{1}{12}t^2)^{\frac{1}{2}}} \exp - \left\{ \frac{(X - \frac{1}{2}Yt)^2}{4t(1+\frac{1}{12}t^2)} + \frac{Y^2}{4t} \right\} \tag{2.1}$$

with $\zeta \to -\ln\rho + 1{\cdot}372$ as $\rho \equiv (X^2+Y^2)^{\frac{1}{2}} \to 0$. A vorticity distribution of the form $\hat{\omega} = A_0\zeta$, with A_0 a proportionality constant, will arise then from a source of vorticity at the surface of the cylinder. One can easily show by application of the divergence theorem to the vorticity equations in (1.1) and (1.7) plus knowledge of the form of ζ as $\rho \to 0$ that

$$A_0 = -\frac{1}{2\pi}\int_0^{2\pi}\left(\frac{\partial\hat{\omega}}{\partial r}\right)_{r=1} d\theta,$$

which is clearly zero. Therefore, since $\hat{\omega}$ must, in addition, satisfy the periodicity condition (1.3), we conclude that far from the cylinder

$$\hat{\omega} \to A_2\,\partial^2\zeta/\partial X^2 \quad \text{as} \quad r \to \infty,$$

A_2 being an undetermined constant.

It has already been shown by Bretherton (1962), however, that, as $r \to \infty$,

$$\zeta \to 3^{\frac{1}{2}}/Y^2 + O(Y^{-4}) \quad \text{if} \quad X/Y = O(1)$$

and

$$\zeta \to (3^{\frac{1}{2}}/X^{\frac{2}{3}})\,I(\alpha) + O(X^{-\frac{4}{3}}) \quad \text{if} \quad \alpha \equiv Y/X^{\frac{1}{3}} = O(1),$$

with

$$I(\alpha) \equiv \frac{\Gamma(\frac{4}{3})}{3^{\frac{1}{3}}}\,e^{\frac{1}{9}\alpha^3} - \tfrac{1}{3}e^{\frac{1}{9}\alpha^3}\int_0^{\alpha} e^{-\frac{1}{9}t^3}\,dt,$$

and thus, in the present case, $\hat{\omega}$ remains significant only within a 'vorticity' wake of dimensions $Y = O(X^{\frac{1}{3}})$, where

$$\hat{\omega} = (3^{\frac{1}{2}}A_2/27X^{\frac{8}{3}})\{(\tfrac{1}{3}\alpha^6 + 10\alpha^3 + 30)\,I - (\tfrac{1}{3}\alpha^4 + 8\alpha)\}. \tag{2.2}$$

The term in braces has a maximum at $\alpha = 2{\cdot}45$ and hence, for a given large x, $\hat{\omega}$ will attain its largest absolute value, proportional to $x^{-\frac{8}{3}}$, when

$$y = y_{\max} = 2{\cdot}45x^{\frac{1}{3}}/R^{\frac{1}{3}}. \tag{2.3}$$

It is evident, of course, that the above conclusions apply irrespective of the magnitude of R, provided that x is sufficiently large.

It is also clear from (2.2) that, for fixed r, the change in the stream function across the vorticity wake will be $O(r^{-2})$ as $r \to \infty$, and hence, for purposes of determining ψ far from the cylinder, the presence of this wake can be ignored. Thus, as $r \to \infty$, ψ satisfies Laplace's equation and, in view of (1.2) and (1.3), assumes the form

$$\psi \to \tfrac{1}{2}r^2\sin^2\theta + B\ln r + A + O(1), \tag{2.4}$$

where it can be shown, by integrating the first equation in (1.1) with respect to θ from $-\frac{1}{2}\pi$ to $\frac{1}{2}\pi$ and applying (1.2) to the solution of the resulting ordinary differential equation, that

$$B = \Omega - \tfrac{1}{2} + \int_1^{\infty} g(t)\,dt, \quad A = -\int_1^{\infty} g\ln t\,dt - \tfrac{1}{4}, \quad \text{with} \quad g(r) \equiv -\frac{r}{\pi}\int_{-\frac{1}{2}\pi}^{\frac{1}{2}\pi}\hat{\omega}(r,\theta)\,d\theta. \tag{2.5}$$

We note that A and B exist, since, in view of (2.2), g becomes $O(r^{-\frac{7}{3}})$ as $r \to \infty$.

We next outline the method of solution. After the customary change of variables from (r,θ) to (ξ,η), with

$$\xi \equiv \pi^{-1}\ln r, \quad \eta \equiv \theta/\pi,$$

the pair of equations (1.1), in terms of the 'deviatoric' dependent variables $\hat{\boldsymbol{\psi}}$ and $\hat{\boldsymbol{\omega}}$,† was cast into a finite-difference form using standard formulae of second-order accuracy except as noted in § 3, with boundary conditions

(*a*) $\hat{\psi}_{1j} = -\frac{1}{2}\sin^2\pi\eta_j$, (2.6)

(*b*) $\hat{\omega}_{1j} = (1-2\sin^2\pi\eta_j) - \dfrac{2}{k^2\pi^2}[\hat{\psi}_{2j} + \frac{1}{2}\sin^2\pi\eta_j] + \dfrac{2}{k\pi}(\Omega - \sin^2\pi\eta_j)$,‡ (2.7)

(*c*) $\hat{\omega}_{mj} = 0$, where ξ_m is the location of the artificial outer boundary, (2.8)

(*d*) $\hat{\psi}_{mj} = B\pi\xi_m + A$, (2.9)

where A and B were calculated from (2.5), and

(*e*) the periodicity requirement (1.3) on $\hat{\boldsymbol{\psi}}$ and $\hat{\boldsymbol{\omega}}$.

Thus, in matrix notation, (1.1) becomes

$$(\mathbf{H}+\mathbf{V})\,\hat{\boldsymbol{\psi}} = \mathbf{f}, \tag{2.10}$$

together with a similar expression for the vorticity equation, where $\mathbf{H}\hat{\boldsymbol{\psi}}$ and $\mathbf{V}\hat{\boldsymbol{\psi}}$ are, respectively, the finite-difference approximations to $\partial^2\hat{\psi}/\partial\eta^2$ and $\partial^2\hat{\psi}/\partial\xi^2$, and $\mathbf{f}$ is the forcing matrix containing $\hat{\boldsymbol{\omega}}$, as well as the boundary conditions. With $\mathbf{f}$ assumed known, (2.10) was then solved using the alternating direction implicit (ADI) iteration scheme (Wachspress 1966, p. 173), according to which

$$\hat{\boldsymbol{\psi}}^{\nu+1} = \hat{\boldsymbol{\psi}}^{\nu} + \mathbf{S}^{\nu+1},$$

the residue $S^{\nu+1}$ being computed from

$$(\mathbf{H}+\gamma_h\mathbf{I})\,\mathbf{S}^* = -(\mathbf{H}+\mathbf{V})\,\hat{\boldsymbol{\psi}}^{\nu} + \mathbf{f}, \quad (\mathbf{V}+\gamma_v\mathbf{I})\,\mathbf{S}^{\nu+1} = (\gamma_h+\gamma_v)\,\mathbf{I}\mathbf{S}^*, \tag{2.11}$$

where ν is the iteration index, $\mathbf{I}$ is the unit matrix and γ_v and γ_h are acceleration parameters. A set of four ADI parameters was employed in the cyclical manner.

After calculating a convergent solution for $\hat{\boldsymbol{\psi}}$ corresponding to a given vorticity distribution, an improved vorticity field was obtained from the finite-difference form of the vorticity equation in (1.1) using a single successive over-relaxation (SOR) pass per overall iteration. Specifically, the new field was determined one column at a time, i.e., with $\mathbf{S}$ again denoting the residual and equal to, in this case, $\hat{\boldsymbol{\omega}}^{\text{new}} - \hat{\boldsymbol{\omega}}^{\text{old}}$, S_{ij} was computed for all i at a given j. The vorticity was calculated a column at a time (constant j) and the field swept in the direction of flow (increasing j). Also, in keeping with the standard practice in SOR iterations, new information was continuously fed into the calculations in that, when computing the jth vorticity column during a given pass, the vorticity in the $(j-1)$th column was replaced by

$$\hat{\boldsymbol{\omega}}^{\text{old}}_{i,j-1} + \beta S_{i,j-1}.$$

β was set equal to 1·2 in all cases except when $R = 70$, where, to maintain stability, it was reduced to 0·05. Finally, the 'new' vorticity field was obtained from

$$\hat{\boldsymbol{\omega}}^{\text{new}} = \hat{\boldsymbol{\omega}}^{\text{old}} + \alpha\mathbf{S};$$

the values of the relaxation parameter α that were used are listed in table 1.

† $\hat{\psi}_{ij} \equiv \hat{\psi}(\xi_i, \eta_j)$ and $\hat{\omega}_{ij} \equiv \hat{\boldsymbol{\omega}}(\xi_i, \eta_j)$, where $\xi_i \equiv (i-1)\,k$ and $\eta_j \equiv (j-1)\,h$, k and h being the grid spacings in the ξ and η directions respectively.

‡ From the usual Taylor series expansion for $\hat{\psi}(\xi, \eta)$ about $\xi = 0$.

Reynolds number R	Outer boundary r_m	Grid spacing in η direction h	Grid spacing in ξ direction (in outer region) k (k_2)	Maximum residual $\mathscr{R}_{\max}$	Number of trials J	Number of iterations on last trial N	Under-relaxation parameter α	'Torque' after last trial RT/π
0·047	30·0	0·0357	0·0277	10^{-6}	5	120	0·75	$1{\cdot}338\times10^{-4}$
1·0	30·0	0·0357	0·0277	10^{-6}	4	195	0·50	$1{\cdot}926\times10^{-3}$
10·0	20·0	0·0294	0·0194	10^{-6}	6	152	0·50	$1{\cdot}454\times10^{-3}$
20·0	20·0	0·0111	0·0156	10^{-6}	4	201	0·30	$5{\cdot}86\times10^{-4}$
30·0	15·0	0·00526	0·0149	3×10^{-6}	2	870	0·30	$-6{\cdot}450\times10^{-3}$
40·0	15·0	0·00526	0·0149	5×10^{-6}	2	795	0·30	$-1{\cdot}564\times10^{-3}$
70·0	15·0	0·00434	0·0128	10^{-5}	1	4200	0·10	$3{\cdot}000\times10^{-3}$

TABLE 1. Parameters used for the zero-torque solutions

In summary then, the numerical procedure was as follows.

(i) The parameters R, ξ_m, h, k, Ω, α and β were specified *a priori*, together with the γ_i, the various acceleration parameters of the ADI scheme, and $\mathscr{R}_{\max}$, the maximum residual convergence criterion.

(ii) Initial values were estimated for A and B in (2.9) and for the $\hat{\boldsymbol{\psi}}$ and $\hat{\boldsymbol{\omega}}$ fields.

(iii) The $\hat{\boldsymbol{\psi}}$ field was converged to the present accuracy using the ADI scheme and the 'known' vorticity.

(iv) $\hat{\omega}_{1j}$ was calculated from (2.7).

(v) Using the new value for $\hat{\boldsymbol{\psi}}$, one SOR pass was made on the vorticity equation to obtain $\hat{\boldsymbol{\omega}}^{\text{new}}$.

(vi) A and B in (2.9) were calculated from (2.5) using $\hat{\boldsymbol{\omega}}^{\text{new}}$, and a new value of $\hat{\psi}_{mj}$ was stored.

(vii) The $\hat{\boldsymbol{\psi}}$ and $\hat{\boldsymbol{\omega}}$ fields were tested for convergence, which required that

$$|S_{ij}| < \mathscr{R}_{\max} \quad \text{everywhere}$$

or, in a few cases, that

$$|S_{ij}/\hat{\omega}_{ij}| < \mathscr{R}_{\max}, \quad |S_{ij}/\hat{\psi}_{ij}| < \mathscr{R}_{\max},$$

where S_{ij} is the residual of the corresponding equation and $\mathscr{R}_{\max}$ typically equalled 10^{-6}. The iteration was of course continued until the above criterion was satisfied.

(viii) After a convergent solution had been obtained various consistency checks, to be discussed in the next section, were carried out and the dimensionless torque T exerted on the cylinder by the fluid was computed from

$$T = -\frac{2\pi}{R}\left\{2(\Omega - \tfrac{1}{2}) + \int_0^1 \hat{\omega}(0,\eta)\,d\eta\right\}. \tag{2.12}$$

For the case in which a zero-torque solution was desired, a new value for Ω was estimated and the whole iteration repeated until the bracketed term in (2.12) became less than 10^{-3}.

Listed in table 1 are the numerical values of the various parameters used to obtain a converged solution for $0{\cdot}047 \leqslant R \leqslant 70$.

3. Some unusual numerical difficulties

A number of difficulties were encountered during the course of this investigation which appear to be peculiar to this type of flow problem and, therefore, are worth mentioning.

First of all, owing to the periodicity of the stream-function field, the ADI iteration scheme gave rise to a matrix $\mathbf{H}$ in (2.11) which is singular. This can be seen by noting that all the elements of $\mathbf{H}$ are zero except for those along the diagonal, which are equal to 2, those along the two off-diagonals, which equal -1, and the two elements in the lower left-hand and upper right-hand corners, both of which equal -1. Fortunately though, (2.11) involves not $\mathbf{H}$ by itself, but rather $\mathbf{H} + \gamma_h \mathbf{I}$, with $10^{-2} \leqslant \gamma_h \leqslant 3{\cdot}0$, whose inverse was obtained using a routine given by Evans (1971).

Another difficulty arose from the presence of large velocities, increasing linearly with r, far from cylinder. Specifically, since the convective terms of the vorticity equation contain first derivatives of $\hat{\omega}$ multiplied by the free-stream velocity components $\frac{1}{2}\pi e^{2\pi\xi} \sin 2\pi\eta$ and $\pi e^{2\pi\xi} \sin^2 \pi\eta$, use of the standard central-difference formula for these first derivatives, as is the general practice with elliptic equations, would have violated two of the requirements needed to assure the convergence of the iteration scheme (Mitchell 1969, p. 144), in that the expression for the vorticity at a point as a linear combination involving its nearest neighbours would have contained negative coefficients at large ξ and the difference-operator matrix would not have been diagonally dominant. Both of these difficulties were solved through the use, in lieu of central differences, of 'first-order accurate' expressions involving upstream information for the first derivatives of vorticity in the region far from the cylinder where the free-stream velocities dominate the inertia terms. This was not a surprising remedy because this type of finite differencing is a standard one for parabolic equations in which the convective terms dominate.

The third difficulty resulted from the fact that, with increasing Reynolds number, the region of closed streamlines became very thin, which meant that the grid spacing in the ξ direction had to be chosen fine enough near the cylinder in order that the derivatives would be approximated properly. Thus, for $R \geqslant 20$, two grid spacings k_1 and k_2 were used, the former corresponding to the region adjacent to the cylinder and the latter to the remaining portion of the flow field, but since the discontinuity in the spacing introduced additional truncation errors in the second derivatives, the ratio k_2/k_1 was held to a value of 2 or 3 (Forsythe & Wasow 1967, p. 188). This complication, along with the decision to retain the calculated values for $\hat{\psi}$ and $\hat{\omega}$ in the high-speed core, significantly reduced the maximum Reynolds number for which a reliable solution could be obtained. For example at $R = 70$, 16 560 grid points were used in the flow field and 4200 iterations were required (or 1·5 h of CDC 7600 computer time) before a convergent solution was attained.

4. Consistency tests and error-analysis results

After a convergent solution for zero torque had been obtained, the following consistency tests were performed to determine the reliability of the results.

(i) The value ξ_m of ξ at the outer boundary was increased by a factor of nearly 2 and the coefficients A and B from (2.5) were compared with the earlier values. As expected, very little change in the coefficients was found from this test since the major contribution to the integrals occurs near the cylinder, the vorticity wake contributing a negligible amount. Actually, after the solutions had been converged, it was found that the grid structure far from the cylinder, with $\Delta\theta$ growing as r, was too coarse relative to the thickness of the vorticity wake, and thus, the vorticity in this region was found to be significantly smaller than should have been the case. Fortunately, this error should have had little effect on the solution near the cylinder, i.e. for $1 \leqslant r < 10$, since the wake lies 'downstream' of the cylinder and the vorticity outside of this wake is essentially zero.

(ii) A standard test of numerical difference approximations involves halving

the grid spacing throughout the flow field and comparing the two sets of solutions. It is then generally assumed that, if the results change only slightly, the original grid spacing was sufficiently small accurately to approximate the derivatives. This was found to be the case in the present work where, for $R = 0{\cdot}047$, $1{\cdot}0$ and 10, a new solution was obtained for the entire flow field with grid spacings $\frac{1}{2}h$ and $\frac{1}{2}k$. At the higher Reynolds numbers, the storage requirements of the computer would not allow us to calculate anew the complete flow field, and instead a new solution was converged only near the cylinder using grid spacings $\frac{1}{2}h$ and $\frac{1}{2}k$ and the previously calculated values for the stream function and the vorticity at the new outer boundary $r_m \approx 5{\cdot}0$. A complete discussion of this process has been given by Leal (1973).

(iii) The flux of vorticity (A_0, following 2.1), which should vanish for a periodic flow, was calculated on the cylinder surface and was always found to be negligibly small.

(iv) Another check involved computing the change in the total head $\mathscr{H}$, where

$$\mathscr{H} \equiv p + \tfrac{1}{2}\mathbf{u}.\mathbf{u}, \tag{4.1}$$

p being the pressure and $\mathbf{u}$ the velocity vector, along a closed path enclosing approximately two-thirds of the flow field and consisting of two segments of constant ξ and two segments of constant η. Clearly, a necessary condition for the consistency of the solution is that the net change in $\mathscr{H}$ along the closed path be zero, where, from the Navier–Stokes equation

$$\mathbf{u} \times \boldsymbol{\omega} = \nabla\mathscr{H} + \mathscr{R}^{-1}\nabla \times \boldsymbol{\omega}, \tag{4.2}$$

it can easily be shown that along a path of constant η

$$\mathscr{H}(\xi_2) - \mathscr{H}(\xi_1) = \int_{\xi_1}^{\xi_2} \left\{ -\frac{1}{R}\frac{\partial \hat{\omega}}{\partial \eta} - (\hat{\omega} - 1)\left[\frac{\partial \hat{\psi}}{\partial \xi} + \pi e^{2\pi\xi} \sin^2 \pi\eta\right]\right\} d\xi, \tag{4.3}$$

and that for a path of constant ξ

$$\mathscr{H}(\eta_2) - \mathscr{H}(\eta_1) = \int_{\eta_1}^{\eta_2} \left\{ \frac{1}{R}\frac{\partial \hat{\omega}}{\partial \xi} - (\hat{\omega} - 1)\left[\frac{\partial \hat{\psi}}{\partial \eta} + \tfrac{1}{2}\pi e^{2\pi\xi} \sin 2\pi\eta\right]\right\} d\eta. \tag{4.4}$$

In the present case the sum of the head losses for the closed path was found to be always very small, i.e. the total head loss was approximately 1–2 % of the average magnitude for the four segments of the curve.

(v) It can be shown that the dimensionless torque T can be computed from

$$T = \frac{1}{R}\int_0^{2\pi} \left[\frac{1}{r}\frac{\partial \psi}{\partial r} - \frac{\partial^2 \psi}{\partial r^2} + \frac{1}{r^2}\frac{\partial^2 \psi}{\partial \theta^2} + R\frac{1}{r}\frac{\partial \psi}{\partial \theta}\frac{\partial \psi}{\partial r}\right] d\theta, \tag{4.5}$$

where the integration is along any path of constant $r \geqslant 1$. The above integral, which reduces to (2.12) when $r = 1$, was evaluated for various r ranging from 5 to 8, and was always found to lie within a few per cent of its value as obtained from (2.12).

An approximate error analysis was performed on the solution at $R = 10$ and 70 to determine the discretization error. It was concluded that, near the cylinder,

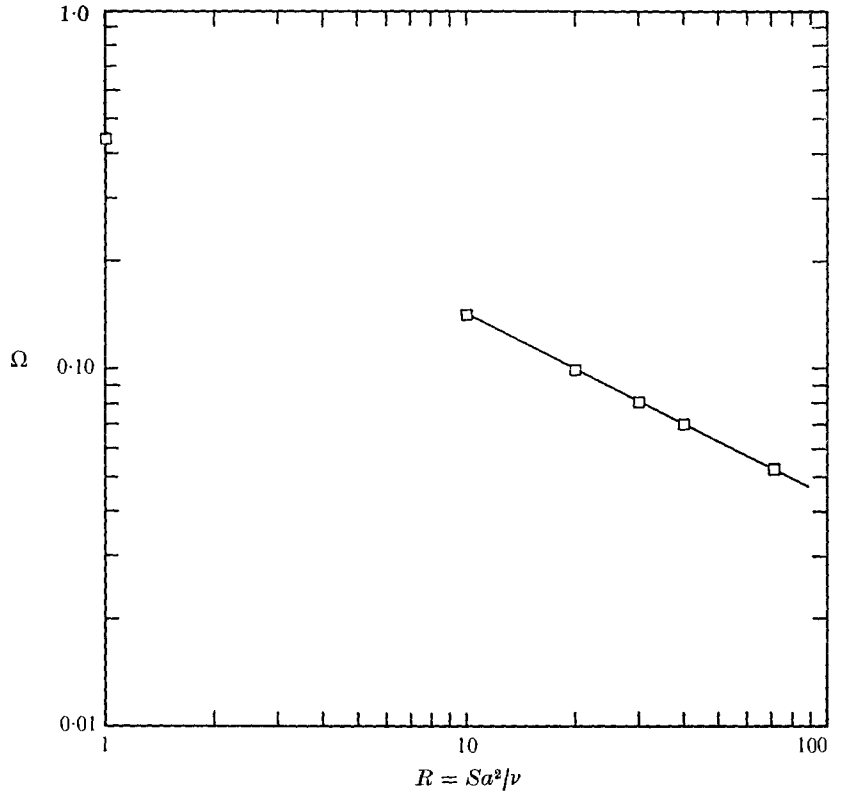

FIGURE 4. The angular speed of a freely rotating cylinder at moderate R.

where central differences were employed, the maximum error in the vorticity field was 1 % and in the stream-function field 0·3 % at $R = 10$, and 0·2 % and 0·05 %, respectively, at $R = 70$. Far from the cylinder, where larger truncation errors are created owing to the use of upstream differences to approximate the first derivatives of vorticity, the maximum error in the vorticity field was 6 % and in the stream-function field 0·3 % at $R = 10$, and 4 % and 0·1 %, respectively, at $R = 70$. All these errors refer to the 'deviatoric' field $\hat{\omega}$ and $\hat{\psi}$.

5. Results for zero torque

Using the technique described above, numerical solutions to the Navier–Stokes equations were obtained at Reynolds numbers of 0·047, 1·0, 10, 20, 30, 40 and 70. As seen in figure 4, Ω was found to decrease monotically with R, which was to be expected for the reasons given in the introduction, and to become proportional to $R^{-\frac{1}{2}}$ in agreement with the predictions of a standard boundary-layer analysis. It is surprising though to note that this last relation appears to hold with remarkable accuracy for values of R as low as 10.

A comparison between the numerical results at $R = 0{\cdot}047$ and the corresponding 'inner' solution (1.6) given analytically by Robertson & Acrivos (1970) is shown in table 2, where θ_s, r_s and ψ_s are the values of the variables at the

Parameter	Inner solution	Numerical solution
Ω (for $T = 0$)	0·49316	0·4932
ψ_s	0·1755	0·1805
θ_s	0·0058	0·0097
r_s	2·428	2·5815

TABLE 2. Comparison of results at $R = 0{\cdot}047$

stagnation points, and in figures 2 and 5 (a), whence it is evident that these agree closely for $r < 4{\cdot}0$ and that, as expected, the inner solution becomes inaccurate for large r. Note also the existence of a stagnation point in the flow, marked by a cross in figure 5 (a), which is a saddle-point in the stream-function field and a characteristic feature of all solutions for non-zero R.

The evolution of the flow and the equi-vorticity pattern with increasing R is depicted in figures 5–8†, from which it becomes apparent that, in at least a qualitative sense, many of the gross aspects of the flow approach those of the inviscid solution (1.9), with $b = \frac{1}{2}$, shown in figure 3. To illustrate further this similarity the streamlines separating the forward from the returning flow have been plotted in figures 9 and 10, the former containing the sets for $R = 0{\cdot}047$, 1·0 and 10, the latter those for $R = 10$, 20, 40, 70 and ∞, with $R = \infty$ denoting the inviscid solution. This last plot also depicts the growth of the region of return flow at large distances from the cylinder. It is surprising to note that the width of this wake at a given large r reaches a maximum at $R \sim 20$ and then decreases monotonically with R towards that for the inviscid solution.

Another interesting plot is that in figure 11, where the calculated values for A and B, the coefficients of (2.9), and the value of ψ at $r_m = 30$ are shown as functions of R together with their corresponding limiting forms for small and for large R obtained, respectively, from the 'outer' solution of Robertson & Acrivos (1970) and from (1.9) with $b = \frac{1}{2}$. Again it is evident that the numerically determined coefficients appear to approach those of the inviscid solution as $R \to \infty$. Note that the circulation around a circle of large r, which is proportional to the magnitude of B, has a maximum at a Reynolds number of approximately 4.

The major differences between the numerical results at the higher Reynolds numbers and those of the $R = \infty$ solution occur, of course, near the cylinder and specifically within the region of closed streamlines. To begin with, it is evident from figures 5 (a), 6 (a) and 8 (a) that the streamline pattern obtained numerically has a single stagnation point in the half-plane at a value of $\theta = \theta_s$, which, as shown in figure 12, appears to asymptote to 20°, in contrast to the two stagnation points of the inviscid solution, which lie on the cylinder at $\theta = \pm 45°$. It is of interest though that δ_s, the distance of the numerically determined stagnation point from the surface of the cylinder, and ψ_s, the value of the stream function at that point, both approach zero, approximately as $R^{-\frac{1}{2}}$ and R^{-1}, respectively, in agreement

† The thinness of the region rendered it impossible to draw the limiting closed streamline around the cylinder for $R = 70$.

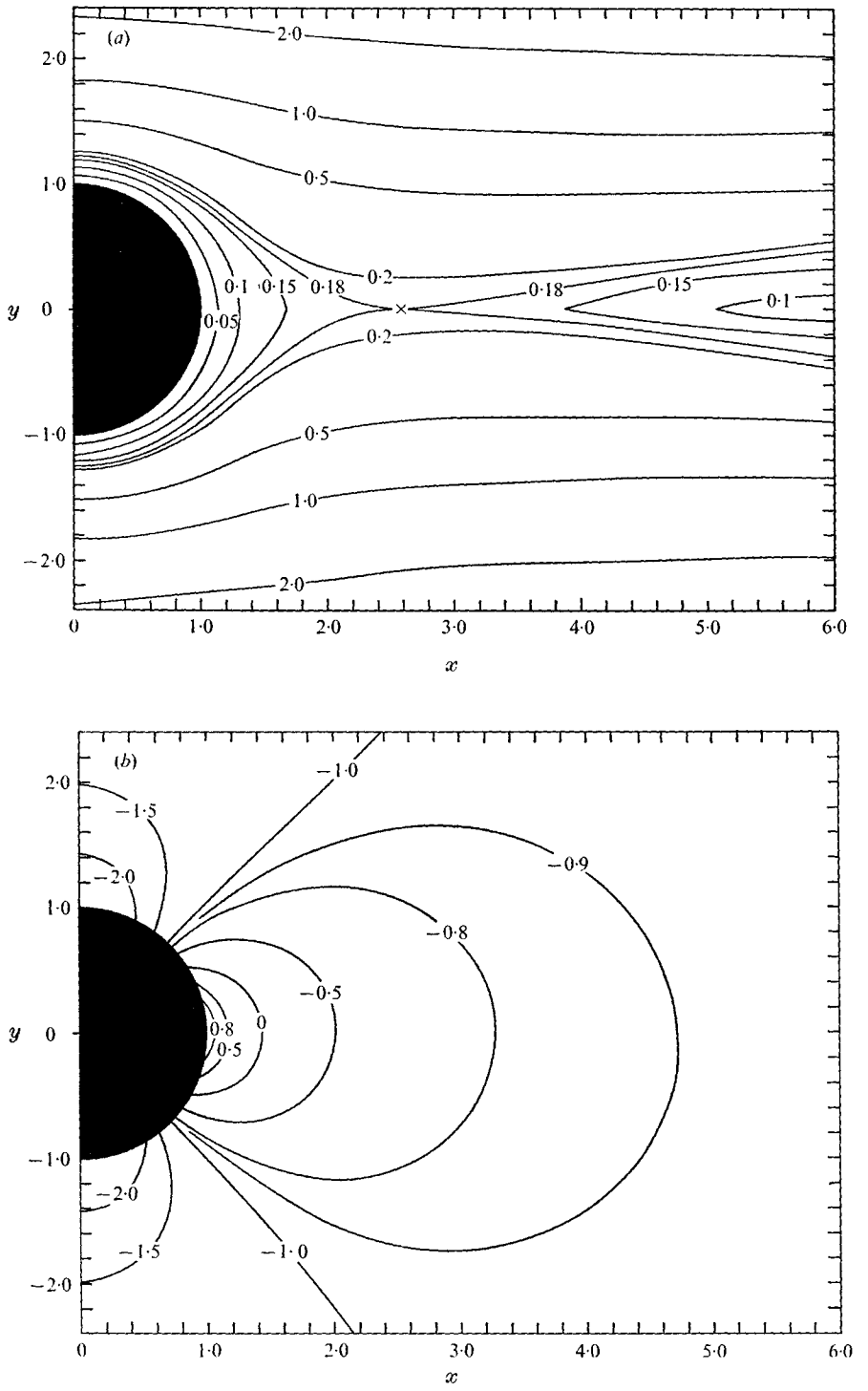

FIGURE 5. (*a*) Stream-function field and (*b*) vorticity field for zero torque, $R = 0{\cdot}047$ and $\Omega = 0{\cdot}4932$, from numerical calculations.

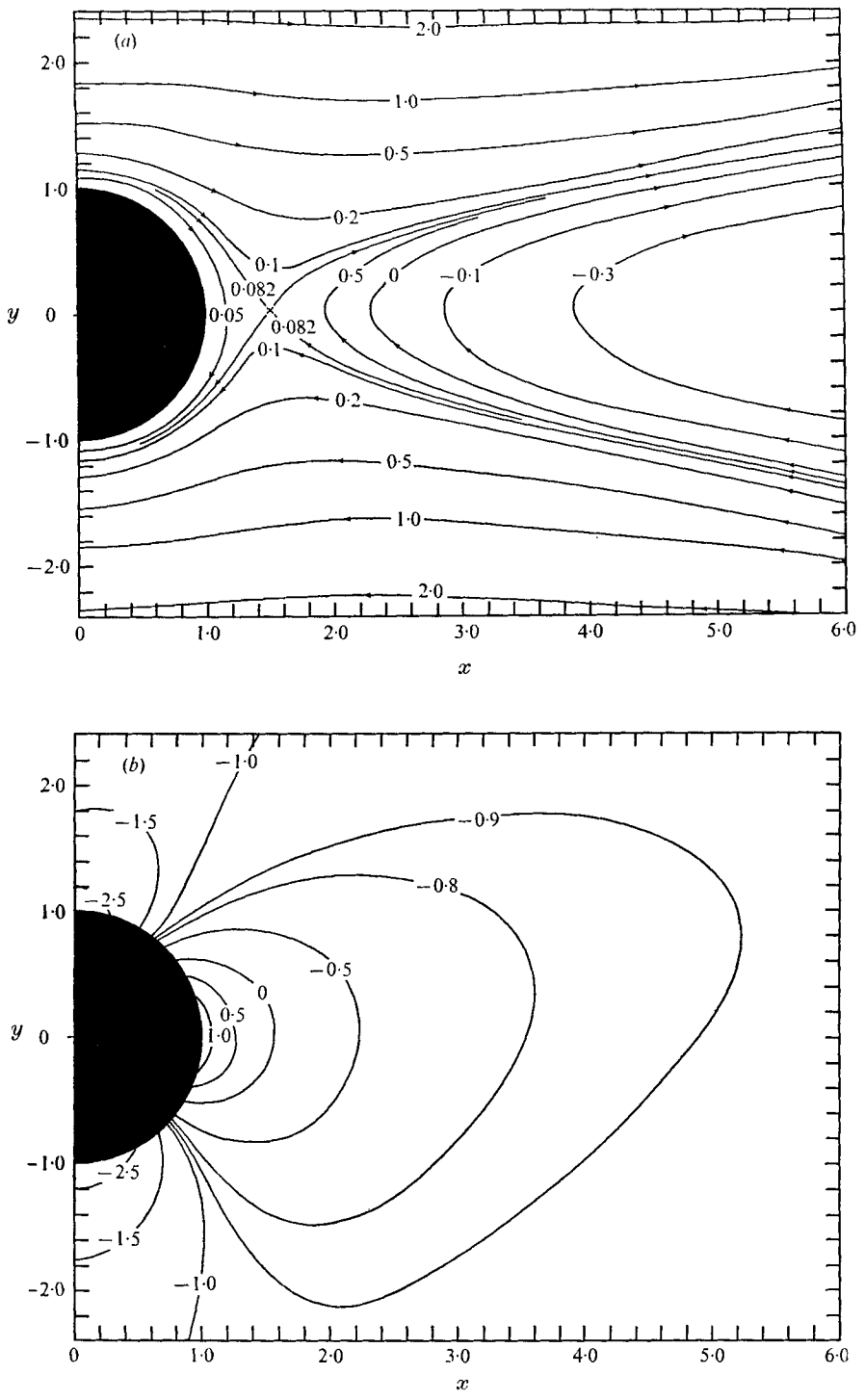

FIGURE 6. (*a*) Stream-function field and (*b*) vorticity field for zero torque, $R = 1{\cdot}0$ and $\Omega = 0{\cdot}438$.

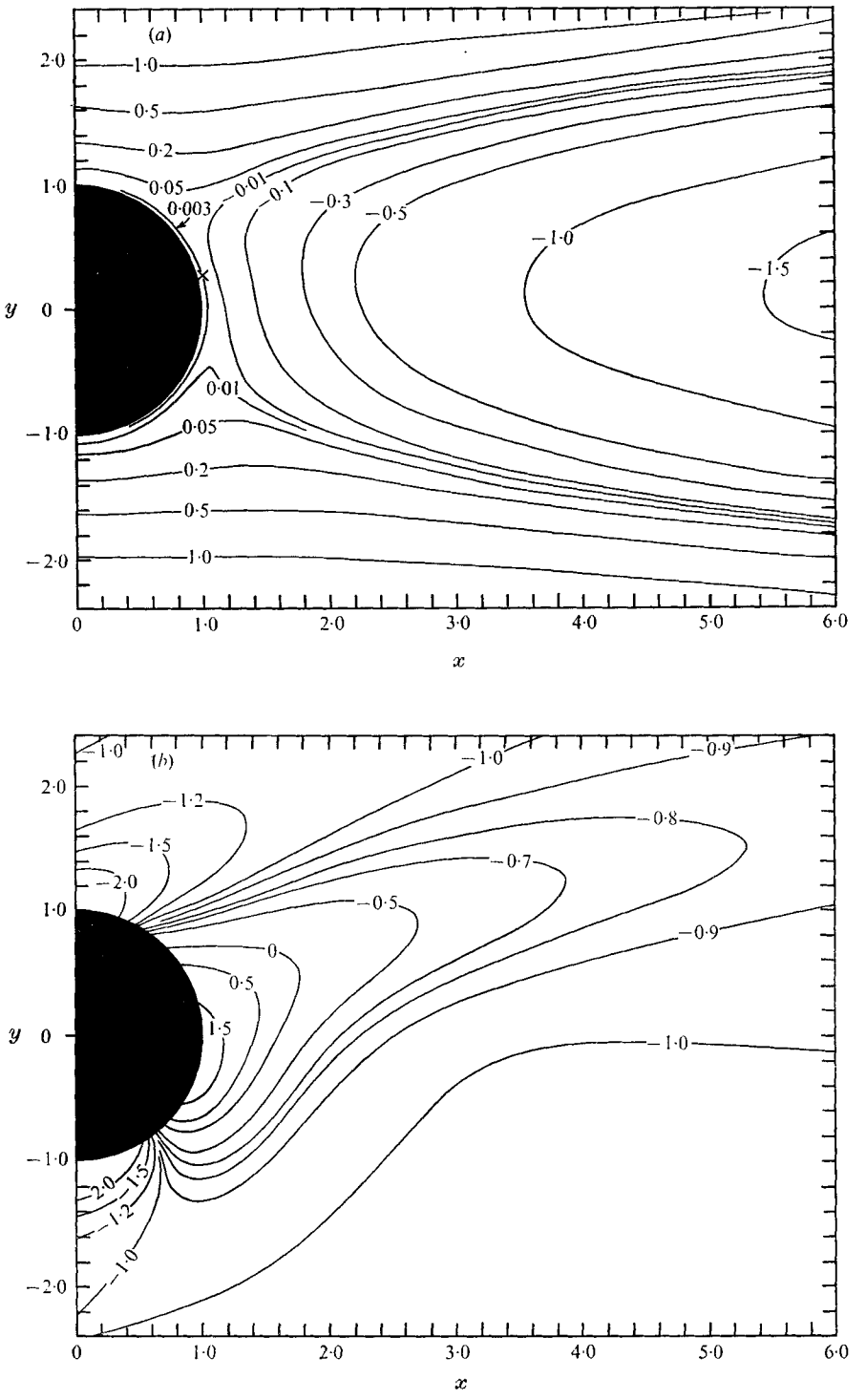

FIGURE 7. (*a*) Stream-function field and (*b*) vorticity field for zero torque, $R = 10{\cdot}0$ and $\Omega = 0{\cdot}141$.

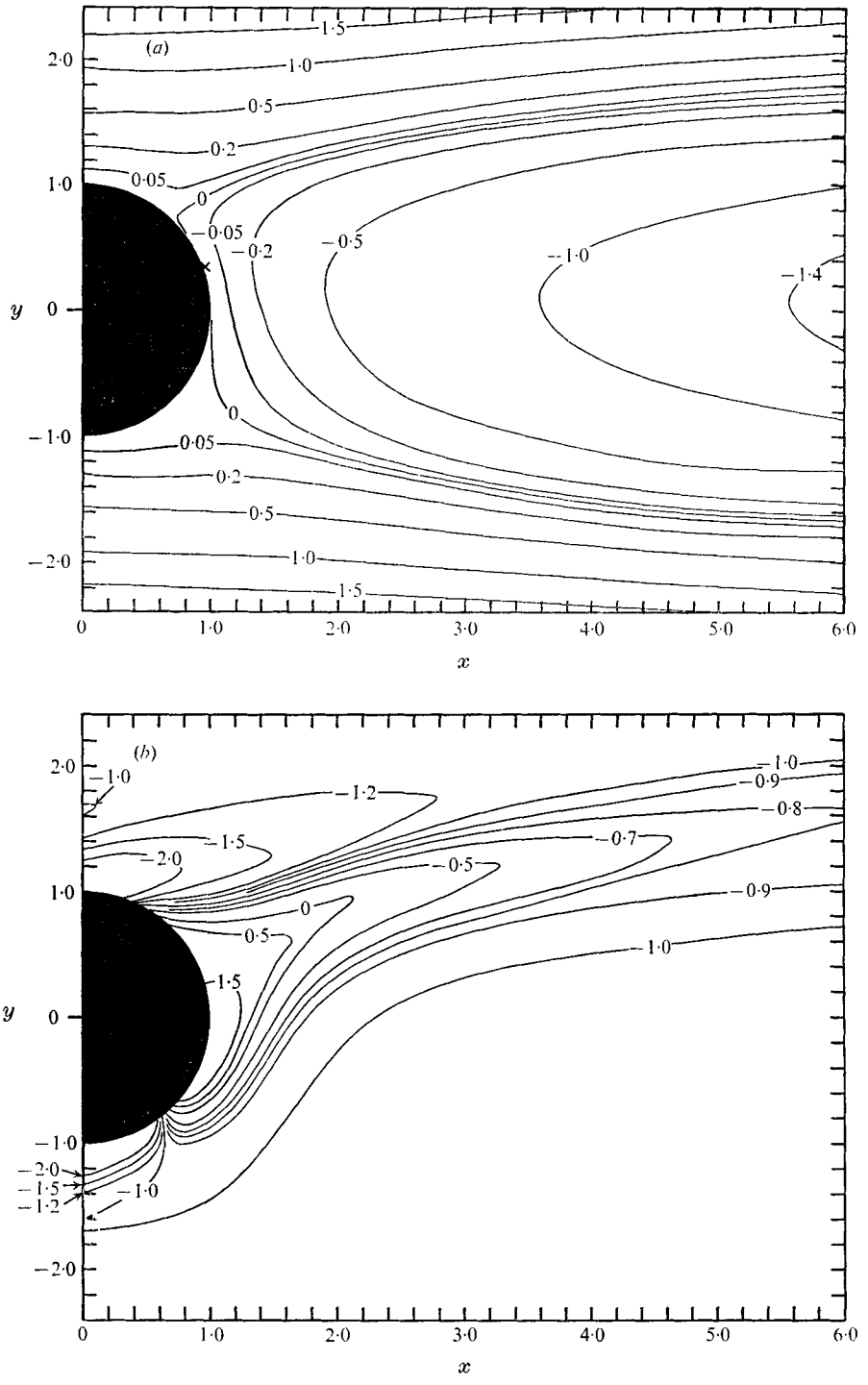

FIGURE 8. (*a*) Stream-function field and (*b*) vorticity field for zero torque, $R = 70{\cdot}0$ and $\Omega = 0{\cdot}0525$.

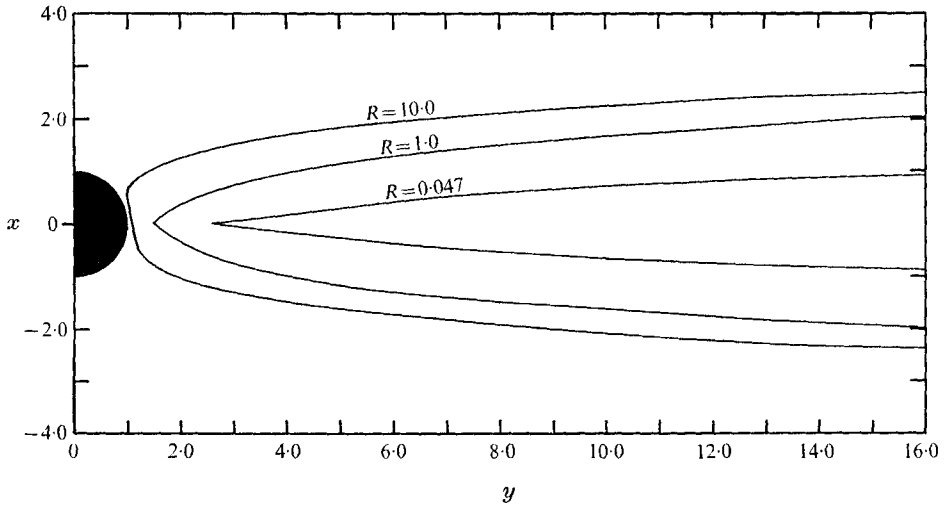

FIGURE 9. The location of the dividing streamline for $0{\cdot}047 \leqslant R \leqslant 10$ and for zero torque.

with the predictions of boundary-layer theory and the fact that Ω is proportional to $R^{-\frac{1}{2}}$.

The most significant difference between the numerical calculations and the inviscid solution, however, is brought out by the corresponding pressure profiles on the cylinder, which are plotted in figures 13 and 14 as a function of η, with p the dimensionless pressure relative to that at $\theta = \frac{1}{2}\pi$, i.e. the relative pressure divided by $\rho S^2 a^2$, ρ being the density and $\bar{p} = pR$. Clearly, the adverse pressure gradient impressed on the flow near the cylinder at $R = 40$ and 70 is much less than that for the inviscid solution. Another difference is that whereas, as mentioned in the introduction, a standard boundary-layer calculation using the inviscid pressure profile would predict the occurrence of boundary-layer separation at $\theta = 45° \pm 36°$, no 'separation' is evident in the numerical solutions even at $R = 70$. Of course, one might be tempted to predict that the agreement between any new numerical results and those of the inviscid solution plus its associated boundary layer would become noticeably better with increasing R, but unfortunately, at this time, it is not certain that this in fact will be the case.

6. Results for $\Omega = 0$ and boundary-layer calculations

Since, as was remarked in the previous section, the numerical solution for zero torque did not show the expected presence of boundary-layer separation even at $R = 70$, the Navier–Stokes equations were solved numerically at $R = 0{\cdot}047$, 1·0, 10, 20, 40 and 70, but with $\Omega = 0$, in order to find out whether the absence of separation in the former case was due, perhaps, to the non-zero rotational velocity of the cylinder. Again, however, no separation was observed.

Briefly, the overall flow pattern was found to be similar to that of the inviscid solution, figure 3, as well as to that of the Stokes solution with $\Omega = 0$ given by Robertson & Acrivos (1970), in that it contained two stagnation points on the

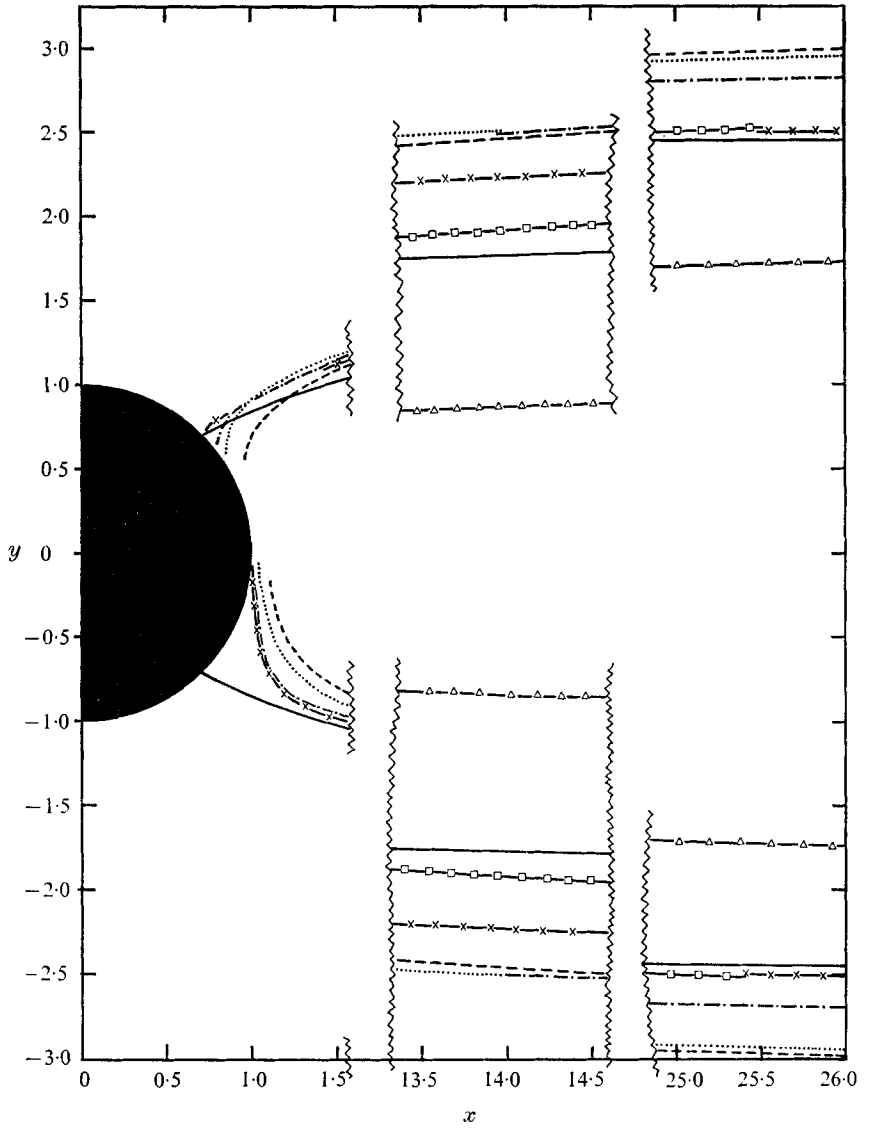

FIGURE 10. The location of the dividing streamline for zero torque at small, intermediate and large distances from the cylinder surface. —△—, $R = 0{\cdot}047$; —□—, $R = 1{\cdot}0$; – – –, $R = 10{\cdot}0$; ····, $R = 20{\cdot}0$; —·—, $R = 40{\cdot}0$; —×—, $R = 70{\cdot}0$; ——, $R = \infty$.

surface of the cylinder plus an open wake. It is of interest that these stagnation points are located at $\theta_s = \pm 30°$ when $R = 0$, at $\theta_s = \pm 45°$ according to the inviscid solutions, but at $|\theta_s| > 45°$ for $R \geqslant 20$. Thus, the curve in figure 15, where θ_s^+ (θ_s^-) denotes the position of the stagnation point in the first (fourth) quadrant, approaches the 45° asymptote from above.

In spite of the absence of closed streamlines near the cylinder, however, the pressure profile at $r = 1$ for a given R was found to be essentially the same as that for the earlier solution with zero torque, a fact illustrated in figure 14 for $R = 70$.

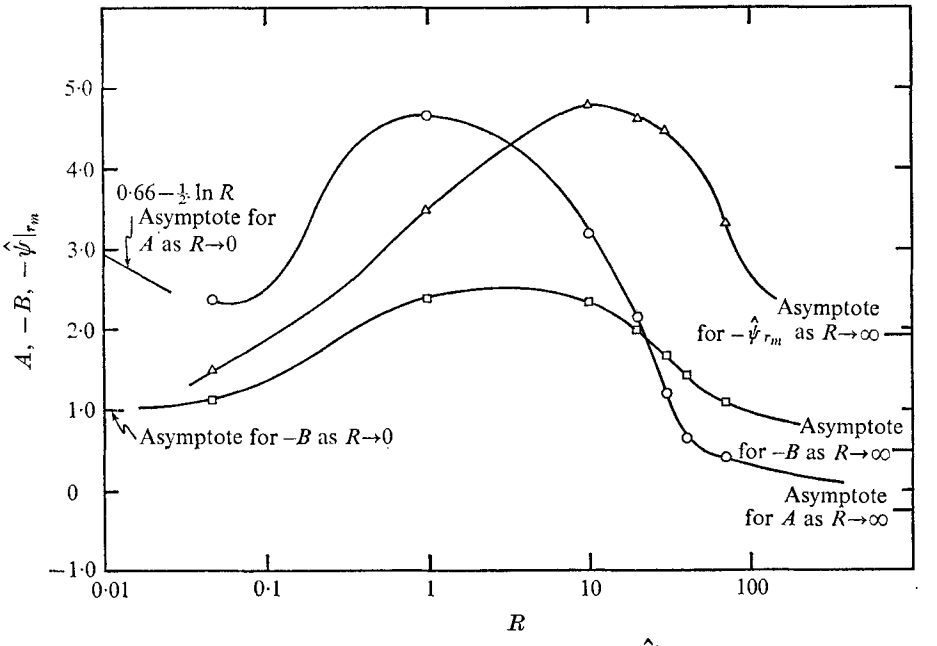

FIGURE 11. The converged values of A, B and $\hat{\psi}|_{r_m}$ ($r_m = 30$) from the zero-torque solutions. ○, A; □, B; △, $\hat{\psi}$ at $r_m = 30$.

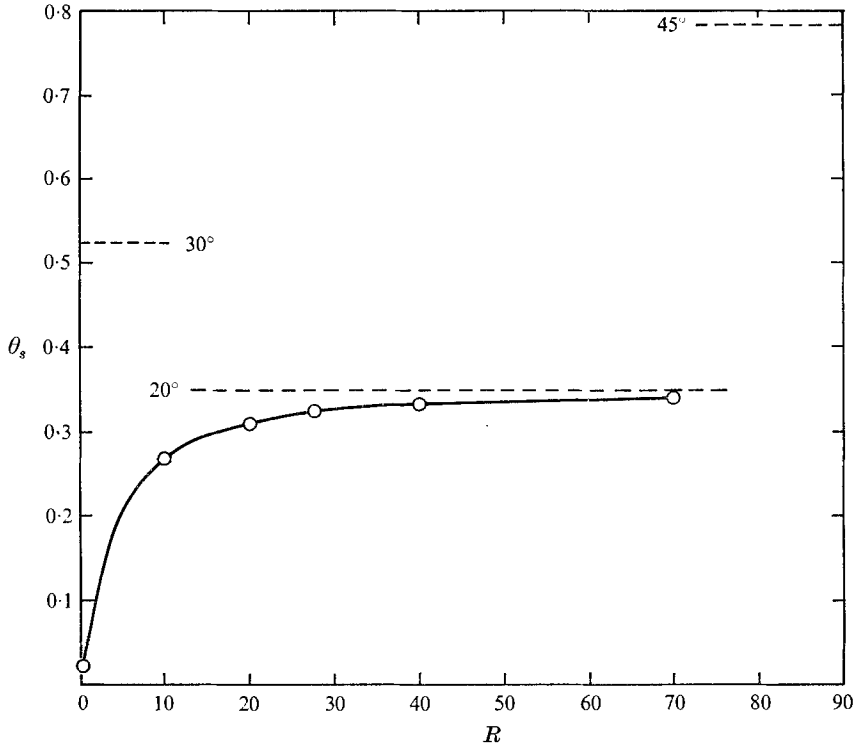

FIGURE 12. The value of θ at the fluid stagnation point for R between 1 and 70 and at zero torque.

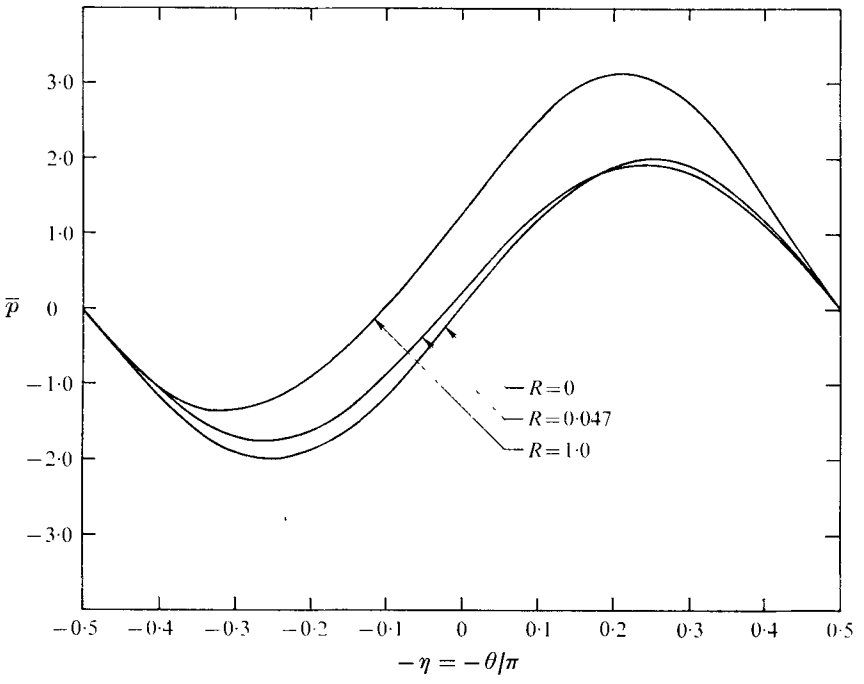

FIGURE 13. Scaled pressure $\overline{p} = pR$ on the surface of the cylinder relative to $\overline{p}$ at $\theta = \frac{1}{2}\pi$, for $0 \leqslant R \leqslant 1{\cdot}0$.

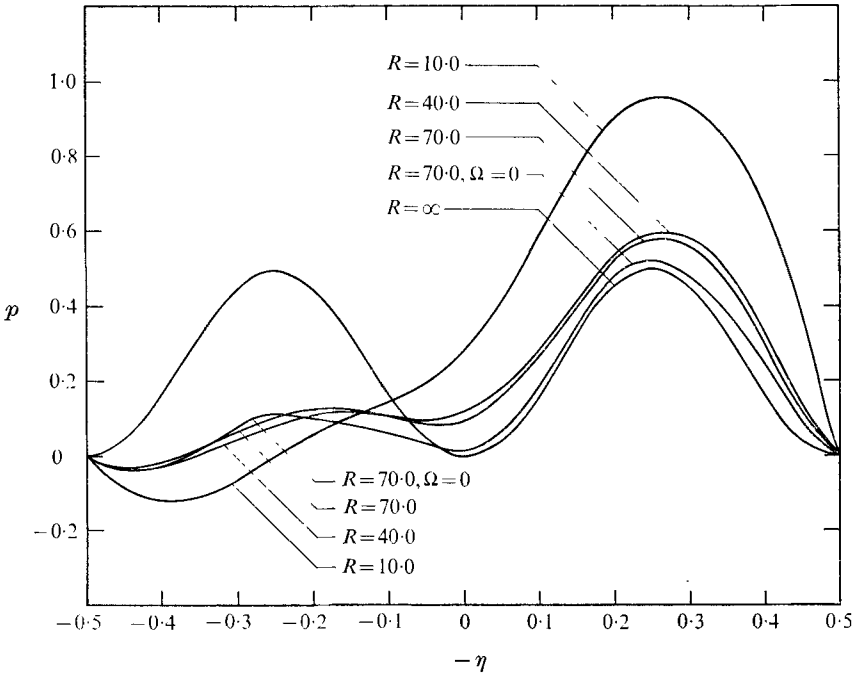

FIGURE 14. Pressure on the surface of the cylinder relative to p at $\theta = \frac{1}{2}\pi$, for $10 \leqslant R \leqslant 70$, and for zero torque except where noted $\Omega = 0$.

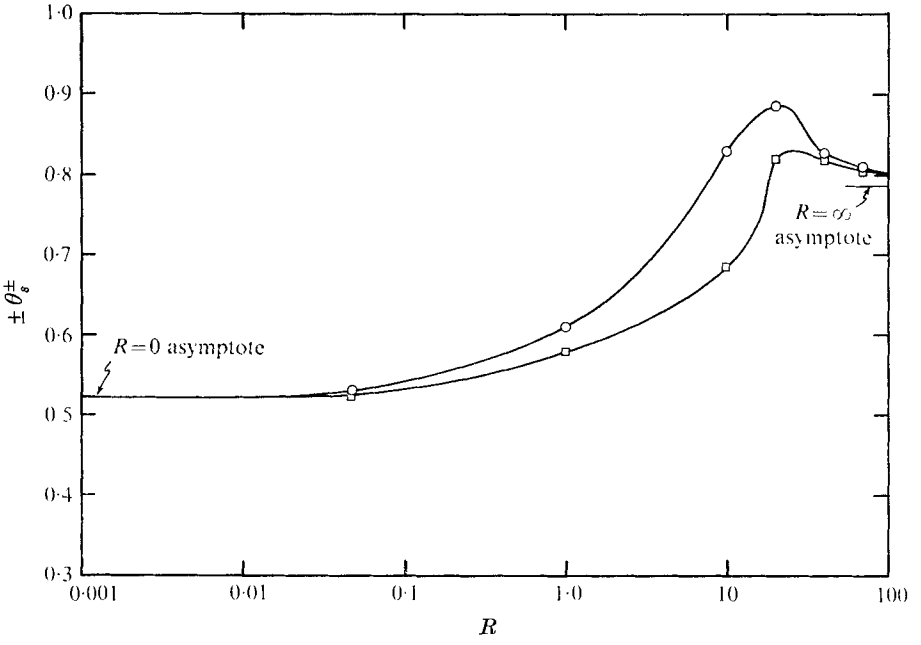

FIGURE 15. The θ co-ordinate of the point of intersection of the $\psi = 0$ curve with the surface of the cylinder (a stagnation point). ○, θ_s^+, for $0 < \theta < \frac{1}{2}\pi$; □, θ_s^-, for $-\frac{1}{2}\pi < \theta < 0$. $\Omega = 0$.

It is perhaps worth reporting that, although no boundary-layer separation was encountered in the numerical solution of the Navier–Stokes equations for values of R up to 70, a solution of the boundary-layer equations using the pressure profile of figure 14, corresponding to $R = 70$ and $\Omega = 0$, produced separation at $\theta = 66{\cdot}6°$.† This suggests that, in this case at any rate, higher-order boundary-layer effects are significant even at $R = 70$, which, of course, is hardly surprising.

Finally, the dimensionless torque T in (2.12), which equals $2\pi/R$ as $R \to 0$ and is $O(R^{-\frac{1}{2}})$ for $R \gg 1$, is shown in figure 16, where the two limiting curves are connected by a dashed line in the transition region $1 < R < 10$.

7. Conclusions

It is evident from what has been presented that the effects of inertia forces on the shear flow past the freely rotating cylinder are quite dramatic at even small Reynolds numbers and result, for example, in the appearance of a stagnation point in the flow, a reduction in the size of the closed-streamline region and in the creation of a 'wake' when the stream function attains negative values. It would be expected, therefore, that this altered flow field will significantly change the rates of heat and mass transfer from the cylinder, compared with those obtained from the $R \equiv 0$ flow.

† The method employed to solve the boundary-layer equations was that of Smith & Clutter (1963) with an implicit iterative scheme replacing the predictor–corrector, three-point interpolation procedure.

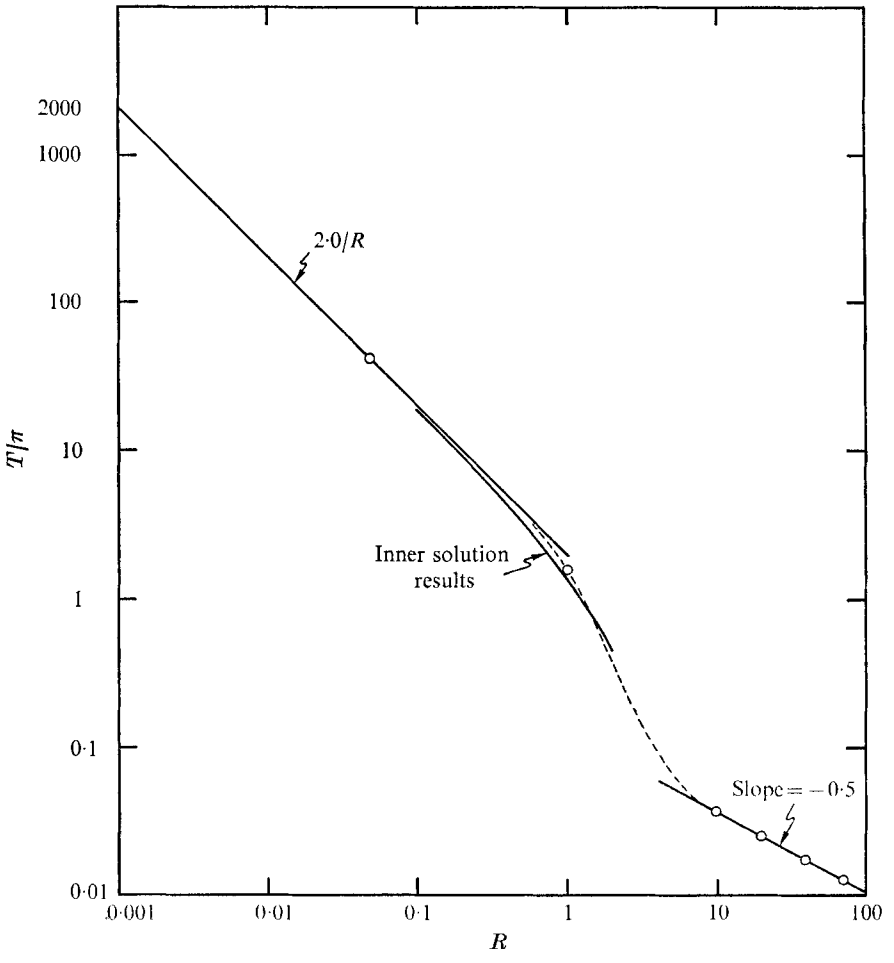

FIGURE 16. The torque on the stationary cylinder at low and high R.
– – – –, smooth interpolation curve.

The fact that in the freely rotating case Ω is proportional to $R^{-\frac{1}{2}}$ for $R > 10$ would lead one to expect that the flow would attain a boundary-layer-type structure for values of R not much larger than $O(1)$. However, although this was found to be the case in many respects, the computed pressure profile is seen to deviate substantially from that of the inviscid solution. Also, even at $R = 70$, the numerical results did not show any flow separation from the surface of the cylinder as would be expected on the basis of a boundary-layer calculation using either the inviscid or the numerically determined pressure profile. Thus, it would appear that a Reynolds number of 70 is not quite large enough to reveal unambiguously the nature of the steady flow as $R \to \infty$, although there are indications that at least some of the features of such an asymptotic flow pattern will be similar to those of the symmetric inviscid solution (1.9) with $b = \frac{1}{2}$.

This work was supported in part by a grant from the National Science Foundation, a grant from NASA-Ames to Stanford University on 'Computational Fluid Mechanics' and by an N.S.F. Traineeship to C.A.K. The major portion of computational work was performed at the National Center for Atmospheric Research, Boulder, Colorado, which is supported by the National Science Foundation.

REFERENCES

BRETHERTON, F. P. 1962 Slow viscous motion round a cylinder in a simple shear. *J. Fluid Mech.* **12**, 591.

COX, R. G., ZIA, I. Y. Z. & MASON, S. G. 1968 Particle motions in sheared suspensions. XXV. Streamlines around cylinders and spheres. *J. Colloid & Interface Sci.* **27**, 7.

EVANS, D. J. 1971 The numerical solution of the fourth boundary value problem for parabolic partial differential equations. *J. Inst. Math. Applics.* **7**, 61.

FRANKEL, N. A. & ACRIVOS, A. 1968 Heat and mass transfer from small spheres and cylinders freely suspended in shear flow. *Phys. Fluids*, **11**, 1913.

FORSYTHE, G. E. & WASOW, W. R. 1967 *Finite-Difference Methods for Partial Differential Equations*. Wiley.

LEAL, L. G. 1973 Steady separated flow in a linearly decelerated free stream. *J. Fluid Mech.* **59**, 513.

MITCHELL, A. R. 1969 *Computational Methods in Partial Differential Equations*. Wiley.

ROBERTSON, C. R. & ACRIVOS, A. 1970 Low Reynolds number shear flow past a rotating circular cylinder. Part 1. Momentum transfer. *J. Fluid Mech.* **40**, 685.

SCHLICHTING, H. 1968 *Boundary-Layer Theory*, 6th edn. McGraw-Hill.

SMITH, A. M. O. & CLUTTER, D. W. 1963 Solution of the incompressible laminar boundary-layer equations. *A.I.A.A. J.* **1**, 2062.

WACHSPRESS, E. L. 1966 *Iterative Solution of Elliptic Systems*. Prentice-Hall.